NANOSYSTEMS:
PHYSICS, CHEMISTRY, MATHEMATICS

Original article

Khrapova E.K., et al. *Nanosystems: Phys. Chem. Math.*, 2024, **15** (6), 821–836.
http://nanojournal.ifmo.ru
DOI 10.17586/2220-8054-2024-15-6-821-836

Intermetallic compounds obtained from $Me_3Ge_2O_5(OH)_4$ (*Me* = Mg, Ni, Fe, Co) phyllogermanates: synthesis of single-phase precursors

Ekaterina K. Khrapova, Anastasia A. Ivanova, Demid A. Kirilenko, Andrei A. Krasilin

Ioffe Institute, St. Petersburg, Russia

Corresponding author: Ekaterina K. Khrapova, e.k.khrapova@mail.ioffe.ru

ABSTRACT Typically, intermetallic compounds are prepared by solid-state method at high temperatures. We propose a simple method to obtain intermetallic compounds by reduction in Ar–H_2 atmosphere from precursors. In particular, Co^{2+} and Fe^{2+} oxidation in hydrothermal conditions grants additional experimental challenge. Here, we report successful Fe phyllogermanate synthesis for the first time. We identify general patterns of formation and determine the effect of hydrothermal treatment on phase composition and morphology for the whole series of phyllogermanates. Formation of phyllogermanates under hydrothermal conditions is studied in the 100 – 200 °C temperature range in three hydrothermal media: H_2O, NaOH, Na_2SO_3. The latter inhibits the oxidation of Co^{2+} and Fe^{2+} during the synthesis. An increase in temperature favors to the formation of phase described by three-layers unit cell. Heat treatment in an Ar–H_2 atmosphere allows us to obtain intermetallic compounds and Me_xGe_y alloys, and to establish the temperature regimes of the reduction processes.

KEYWORDS intermetallic compounds, phyllogermanate, hydrothermal synthesis, reduction

ACKNOWLEDGEMENTS The work was financially supported by the Russian Science Foundation (Project No. 23-22-00245, https://rscf.ru/project/23-22-00245/). Powder X-ray diffraction was performed using the equipment of the Engineering Centre of St. Petersburg State Technical University (Technical Institute). TEM studies were performed using equipment of the Federal Joint Research Center “Material science and characterization in advanced technology” supported by the Ministry of Science and Higher Education of the Russian Federation.

FOR CITATION Khrapova E.K., Ivanova A.A., Kirilenko D.A., Krasilin A.A. Intermetallic compounds obtained from $Me_3Ge_2O_5(OH)_4$ (*Me* = Mg, Ni, Fe, Co) phyllogermanates: synthesis of single-phase precursors. *Nanosystems: Phys. Chem. Math.*, 2024, **15** (6), 821–836.

1. Introduction

Class of 1:1 phyllogermanates is a poorly studied, although they are structural analogues of 1:1 phyllosilicates. These phyllosilicates have a unique structure consisting of two sublayers, tetrahedral SiO_4 and octahedral MeO_6. The octahedral sublayer has a larger size compared to the tetrahedral one, which leads to folding into nanoscrolls. [1,2]. This morphology is typical for chrysotile. Lizardite is a platy analog of chrysotile. It has a similar structure but does not fold [3]. The chrysotile structure allows isomorphic substitution in the cation sublattice of Mg^{2+} and Si^{4+} by Ni^{2+} [4–7], Co^{2+} [7–9], Fe^{2+} [7, 10], Fe^{3+} [11, 12], Ti^{4+} [13], Ge^{4+} [14, 15] with preservation of the scrolled morphology or formation of plates. Attempts to obtain phyllosilicates with partial or complete replacement of Si^{4+} by Ge^{4+} have been made for several compounds. $Mg_3Ge_2O_5(OH)_4$ and $Ni_3Ge_2O_5(OH)_4$ phyllogermanates and are the first phyllogermanates obtained on the basis of chrysotile. The substitution of Si^{4+} by Ge^{4+} led to the formation of hexagonal plates [14]. In another related group of layered phyllosilicates $Al_2Si_2O_5(OH)_4$, the substitution of Si^{4+} by Ge^{4+} led to the folding of kaolinite sheet into scrolls with halloysite-like structure. It was possible to obtain multi-walled or single-walled nanotubes, as well as curved nanosheets, by varying the Ge/(Ge+Si) ratio [16]. In another nanotubular phyllosilicate, imogolite $Al_2SiO_3(OH)_4$, the Ge/Si ratio affected the diameter of the nanotubes as well as their length [17].

In this work, phyllogermanates with the stoichiometric formula $Me_3Ge_2O_5(OH)_4$ (*Me* = Mg, Ni, Fe, Co) were selected for study. The structure of such compounds has not been studied in details. The only one that has been determined was $Mg_3Ge_2O_5(OH)_4$. Only for this compound, it was possible to construct a unit cell. It had six layers with some layers shifted by $\pm b/3$, which was also typical for other serpentine compounds, including their polytypes [18]. $Co_3Ge_2O_5(OH)_4$ also had a layered structure, but the number of layers in the unit cell was limited to three [19]. Such a structure and morphology create a number of advantages that make such compounds perspective in catalysis and adsorption application. Advantages include the presence of a large number of surface hydroxyl groups, the provision of a redox cycle through rapid electron transfer, and the control of surface-active centers by changing the number of layers in the particles [20–23]. The most actively studied are cobalt and nickel phyllogermanates, which, in addition to the properties listed, can also be used as anode materials due to the presence of transition elements in their composition [24, 25]. Their electronic [23] and magnetic [19] properties can potentially ensure their applicability in spintronics [26].

It is possible to obtain the corresponding orthogermanates or intermetallic compounds based on phyllogermanates. Although Ge-intermetallic compounds are promising materials for use in semiconductor devices [27, 28] and energy storage devices [29], as well as in various catalytic processes [29–31]. Intermetallic compounds are obtained by solid-state methods requiring high temperatures in most cases [31]. The reduction of Ge and transition elements from a single precursor, in particular phyllogermanates, would allow to obtain intermetallic compounds of a given composition. This article presents a new simple method for the preparation of Ge-intermetallic compounds, consisting of the reduction of phyllogermanates in an Ar–H_2 atmosphere. The synthesis parameters for the preparation studies of Mg, Ni, Co and, in particular, Fe phyllogermanates, which were obtained for the first time, are also presented.

2. Experimental

2.1. Samples preparation

$Me_3^{2+}Ge_2O_5(OH)_4$ (*Me* = Mg, Ni, Co, Fe) phyllogermanates were obtained by reverse coprecipitation followed by hydrothermal treatment. The synthesis was carried out in a glove box under an inert argon atmosphere for Co- and Fe-phyllogermanates. Oxygen-free water was used in the synthesis, obtained by distillation in an inert Ar atmosphere followed by 2 – 3 cycles of vacuum evacuation. All phyllogermanates were obtained according to the general scheme: crystalline GeO_2 (1 g) was dissolved in a 0.3 M NaOH aqueous solution (0.1 L). Then 0.15 M aqueous solution (0.1 L) of the salt ($FeSO_4 \cdot 7H_2O$, $NiCl_2 \cdot 6H_2O$, $CoCl_2 \cdot 6H_2O$ or $MgCl_2 \cdot 6H_2O$) was added dropwise at constant stirring to obtain a molar ratio Me/Ge = 1.5. The precipitate was then washed by decantation until there was negative reaction for chloride ions with $AgNO_3$ solution in the case of Mg and Ni phyllogermanates. Then the precipitate was ground in an agate mortar. Washing to remove impurity ions was not performed to minimize sample contact with oxygen for Co- and Fe phyllogermanates. All samples (0.2 g) placed in 25 mL Teflon crucibles in high-pressure vessels and 20 mL of distilled water or aqueous solutions of 0.1 M NaOH, 0.1 M Na_2SO_3 were added as hydrothermal medium (HTM). Na_2SO_3 was used only for Co- and Fe-phyllogermanates to prevent oxidation during the hydrothermal treatment [9]. The hydrothermal treatment temperatures for all samples were 100, 150, and 200 °C. The holding time was 72 h, and the estimated pressure was 2 MPa. The samples were dried in air at a temperature of 80 °C after the hydrothermal treatment.

The samples were reduced in a tube furnace in an Ar–H_2 flow (5 % vol. H_2) at $T = 900$ °C for 5 h at a heating rate of 10 °/min. The samples were cooled together with the furnace in an inert atmosphere.

2.2. Samples characterization

Powder X-ray diffraction (PXRD) was performed on a Rigaku SmartLab 3 (Japan) with a cobalt anode ($\lambda = 1.789$ Å) and a K_β-filter in the Bragg–Brentano geometry in the range of 5 – 80°, a step of 0.01°, and a shooting rate of 1 °/min. The cathode heating current was 35 mA and the accelerating voltage was 40 kV. X-ray phase analysis was performed using the PDF-2 crystallographic database. The lattice parameters were determined in the Rigaku SmartLab Studio II software package by the direct derivation method [32]. Crystallite size was determined by the WPPF method [33]. Temperature programmed reduction (TPR) was performed on a Chemosorb (Russia). Samples in the form of tablets (0.03 g) were placed in quartz crucibles and heated to $T = 110$ °C at a rate of 10 °/min in an inert argon atmosphere until there was no change in sample mass. The sample was heated to $T = 950$ °C in an Ar–H_2 atmosphere (10 % vol. H_2) at a rate of 10 °/min.

The elemental analysis of the samples was determined by energy-dispersive spectroscopy (EDS) on a FEI Quanta 200 scanning electron microscope (USA) with an X-ray Si(Li) microanalyzer. The morphology of the samples was also determined with this microscope. A transmission electron microscope (TEM) JEM 2100-F Jeol (USA) was additionally used for samples with nano-sized particles. The overage particle size of the basis of 100 particles for each sample was calculated using the ImageJ program [34].

3. Results and discussion

3.1. Products of hydrothermal treatment

Phyllogermanates, as 1:1 analogues of phyllosilicates, had a similar layered structure. They were characterized by partial displacement of the layers with an increase in their number in the lattice. To determine the phase composition and the lattice parameters, one-, two- and three-layer unit cells were constructed based on the three-layer unit cell from [19], with the second layer shifted by $-b/3$. The proposed model was a kind of averaging and reflected the general tendency for the adjacent layers to shift. Based on the processing results, the number of layers in the unit cell could be determined for each sample, as well as the lattice parameters and crystallite size. The phase composition of phyllogermanate samples after hydrothermal treatment in the temperature range of 100 – 200 °C in different hydrothermal media is shown in Fig. 1. Both temperature and hydrothermal media affected the formation of phyllogermanates.

$Mg_3Ge_2O_5(OH)_4$

	H_2O	NaOH
100°C	2L	2L
150°C	2L + 3L	2L + 3L
200°C	2L + 3L	2L + 3L

$Fe_3Ge_2O_5(OH)_4$

	H_2O	Na_2SO_3	NaOH
100°C	3L poor cr.	3L + 2L	3L
150°C	3L	3L	3L + Fe_2O_3
200°C	Fe_2O_3 + Fe_2GeO_4	3L + Fe_2GeO_4	Fe_2O_3 + Fe_2GeO_4

$Ni_3Ge_2O_5(OH)_4$

	H_2O	NaOH
100°C	1L	1L
150°C	2L	2L
200°C	2L + 3L	2L + 3L

$Co_3Ge_2O_5(OH)_4$

	H_2O	Na_2SO_3	NaOH
100°C	2L + 3L	2L + 3L	2L + Co_2GeO_4
150°C	2L + 3L	2L + 3L	3L + Co_2GeO_4
200°C	3L	3L	3L + Co_2GeO_4

FIG. 1. Phase composition of samples obtained in different hydrothermal media in the 100 – 200 °C temperature range (L – layer, poor cr. – poor crystalline)

3.1.1. Mg-phyllogermanate. Crystal structure of Mg-phyllogermanate formed at $T = 100$ °C was described by a two-layer unit cell. The NaOH-HTM sample (Fig. A1, Appendix) possessed higher crystallinity in comparison to the H_2O-HTM sample (Fig. A2, Appendix). Temperature increased up to 150 °C yielded formation of phase described by three-layer unit cell. More active formation of that phase occurred in the H_2O-HTM sample, and it dominated at $T = 200$ °C. Phase described by two-layer unit cell predominated in the NaOH-HTM sample in the whole temperature range. Lattice parameters did not change significantly (Fig. A3, Appendix), and the reduced unit cell volume (the cell volume divided by the number of layers) did not change either with temperature or with hydrothermal medium change (Fig. 2e). Phyllogermanate phase formation occurred already at 100 °C, and then only the number of layers increased with increasing temperature, while the layer structure itself remained mostly unchanged. TEM and SEM micrographs are shown in Fig. 3. All the particles had platy morphology. The particle shape approached hexagonal, and the plates average size increased with increase in temperature. The particle size was 9 ± 4 nm in the H_2O-HTM sample and 25 ± 6 nm in the NaOH-HTM sample at $T = 100$ °C. Temperature increase up to 150 °C yielded increase in particle sizes to 23 ± 7 and 73 ± 30 nm, respectively, and they grew up to 1.7 ± 0.3 μm (H_2O-HTM) and 1 ± 0.2 μm (NaOH-HTM) at $T = 200$ °.

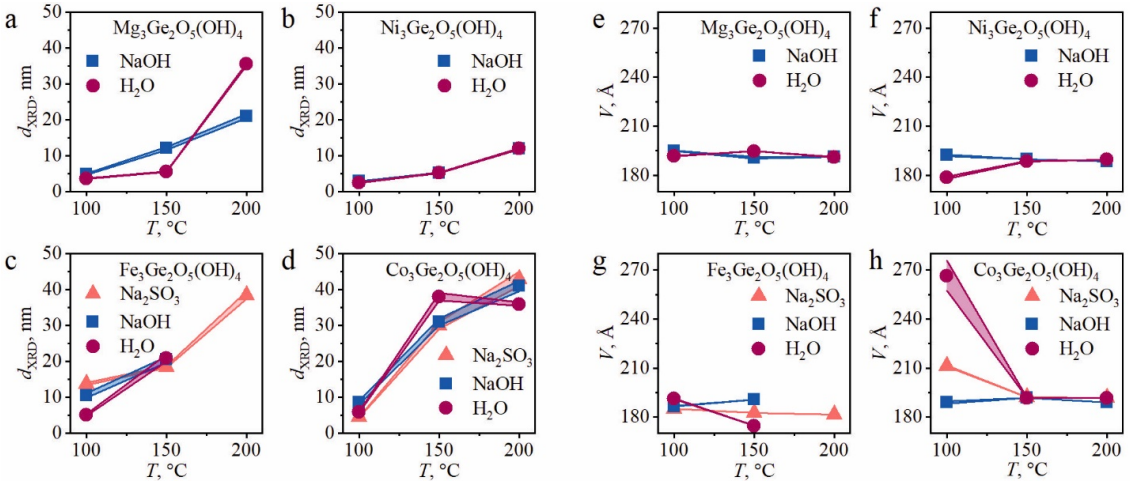

FIG. 2. Crystallite size of samples for all hydrothermal media in the temperature range 100 – 200 °C for: a) $Mg_3Ge_2O_5(OH)_4$; b) $Ni_3Ge_2O_5(OH)_4$; c) $Fe_3Ge_2O_5(OH)_4$; c) $Co_3Ge_2O_5(OH)_4$ and unit cell volume reduced to one layer for all hydrothermal media in the temperature range 100 – 200 °C for: e) $Mg_3Ge_2O_5(OH)_4$; f) $Ni_3Ge_2O_5(OH)_4$; g) $Fe_3Ge_2O_5(OH)_4$; h) $Co_3Ge_2O_5(OH)_4$

Unusual size dependence could be related with concurrent effect of pH and temperature on the particles aggregation and components solubility. It is believed that particles growth occurs via two main mechanisms: dissolution/precipitation (Ostwald ripening) and oriented attachment [35]. The first mechanism involves the gradual growth of large particles due to the dissolution of small ones. In this point of view, increase in components solubility by rising the pH value would promote particles growth, that was observed in practice. Breakage of this trend at high temperature occurred, apparently, because of dramatic increase in both GeO_2 [36] and $Mg(OH)_2$ solubility, so even the large phyllogermanate particles

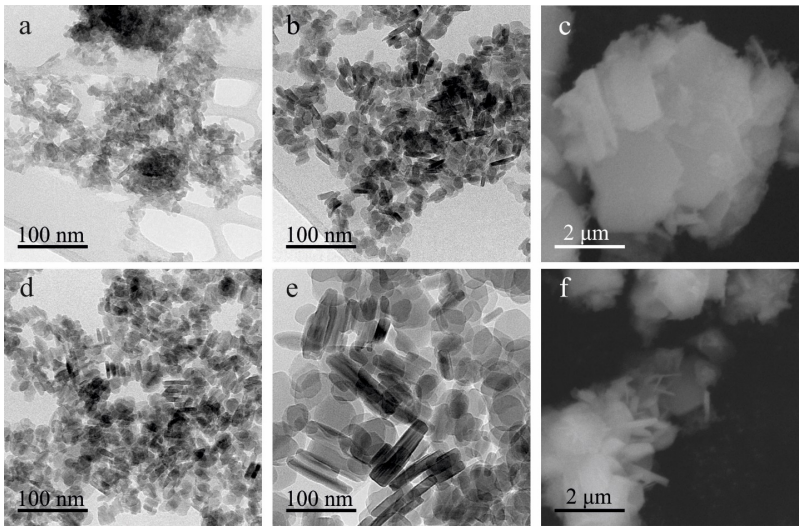

FIG. 3. TEM and SEM micrographs of $Mg_3Ge_2O_5(OH)_4$ in H_2O hydrothermal medium at a) 100 °C (TEM); b) 150 °C (TEM); c) 200 °C (SEM) and in NaOH hydrothermal medium at d) 100 °C (TEM); e) 150 °C (TEM); f) 200 °C (SEM).

began to dissolve. Therefore, a lot of nuclei appeared in bulk of HTM during the cooling step of the high-pressure vessel, resulting in decrease of average particle size. This was indirectly confirmed by the EDS data shown in Table 1. A given Mg/Ge = 1.5 ratio was maintained in the H_2O-HTM sample, while the ratio increased to 1.65 due to partial dissolution of GeO_2 in the NaOH-HTM sample.

On the other hand, the particle size and crystallinity may sharply increase because of oriented attachment. Availability of related surfaces of adjacent particles is key condition for the attachment. Platy particle morphology facilitates this process along *00l* direction thus yielding thick plates and multi-layer polytypes. However, high pH value could inhibit the oriented attachment via increase in ζ-potential (by absolute value) and suspension stability. For example, high concentration of alkali (pH = 13) caused decrease in $Mg(OH)_2$ ζ-potential down to –25 mV [37], that might be the case of the NaOH-HTM sample. As a result, the particles repelled each other and their possibility for the attachment decreased. The crystallite size shown in Fig. 2a gradually increased from 5 to 20 nm for the NaOH-HTM sample. In the H_2O-HTM sample, a sharp jump in the crystallite size was observed at $T = 200$ °C (40 nm). This was apparently due to the active formation of phase described by three-layer unit cells and the emergence of preferential directions of oriented attachment. For phases described by two-layer unit cells, the most intense diffraction maxima corresponded to the *00l* and *h00* directions, which were associated with crystallite growth both along and perpendicular to the layers. Texturing also contributed to the increase in diffraction maxima with 00*l* indices. The appearance of the third layer was characterized by an increase in intensity along the *113* direction, which was also almost perpendicular to the layers in the unit cell.

3.1.2. Ni-phyllogermanate. Ni-phyllogermanate showed similar trends to Mg-phyllogermanate (Fig. 1). However, Ni-phyllogermanate was characterized by the formation of phase described by one-layer unit cell at $T = 100$ °C. Phase described by two-layer unit cell was formed at $T = 150$ °C, and a slight presence of phase described by tree-layer unit cell was observed (Fig. A4 and Fig. A5, Appendix). It was possible that Ni-phyllogermanate required higher temperatures to form phases with multi-layer unit cells, as indicated by the tendency for the number of layers to increase with increase in temperature, but no dependence on the HTM type was observed. Unit cell volume (Fig. 2f) was significantly different for the two hydrothermal media only at $T = 100$ °C. The rest of the lattice parameters were also HTM-independent in the 150 – 200 °C range (Fig. A6, Appendix). The crystallite size in both media gradually increased from 4 to 12 nm with increase in hydrothermal treatment temperature (Fig. 2b). The particles themselves also had the shape of plates. The particles of the NaOH-HTM sample were smaller than 7 nm at $T = 100$ °C (Fig. A7a, Appendix). A significant difference in particle size was observed depending on the HTM type at high temperature. While the average particle size of the H_2O-HTM reached 2 μm and more at $T = 200$ °C (Fig. A7b, Appendix), for individual particles of the NaOH-HTM sample were almost indistinguishable in the SEM. In addition to the reasons discussed for the Mg-phyllogermanate case (including high ζ-potential value of NiO and $Ni(OH)_2$ [38, 39]), greater sensitivity of Ni-containing systems to pH value should be noted for the case of Mg- and Ni-phyllosilicate nanoscrolls formation [40, 41]. Comparing these observations with our previously published paper [15], in which Ni-phyllogermanate particle sizes reached 0.5 μm independently on pH, we are once again convinced of the importance of the role of chemical prehistory in the formation and growth of crystals. Thus, the usage of crystalline compounds mechanical mixtures ($Ni(OH)_2$ and GeO_2 [15]) demanded for comparatively high temperatures (240 °C) to start recrystallization, and particle sizes were predetermined by the less soluble compound.

TABLE 1. Elemental composition of phyllogermanates for all hydrothermal media in the 100 – 200 °C temperature range

$Mg_3Ge_2O_5(OH)_4$					
HTM	T, °C	Element content, at.%			Mg/Ge
		Mg	Ge	O	
H_2O	100	22.79±0.21	15.36±0.15	61.86±0.16	1.48±0.03
	150	24.31±0.21	15.50±0.14	60.19±0.33	1.57±0.03
	200	24.41±0.19	16.52±0.31	59.07±0.47	1.48±0.04
NaOH	100	24.54±0.18	14.84±0.15	60.62±0.29	1.65±0.03
	150	25.06±0.16	15.23±0.23	59.71±0.34	1.65±0.04
	200	25.36±0.23	15.42±0.11	59.26±0.30	1.64±0.03
$Ni_3Ge_2O_5(OH)_4$					
HTM	T, °C	Element content, at.%			Ni/Ge
		Ni	Ge	O	
H_2O	100	22.20±0.45	15.45±0.04	62.36±0.43	1.44±0.03
	150	26.76±0.61	18.40±0.31	54.84±0.33	1.45±0.06
	200	29.16±0.35	19.46±0.45	51.38±0.67	1.50±0.05
NaOH	100	27.48±0.70	17.30±0.07	55.21±0.73	1.59±0.05
	150	24.87±0.96	19.13±0.05	56.00±0.95	1.30±0.05
	200	27.08±0.83	19.46±0.11	53.46±0.77	1.39±0.05
$Co_3Si_2O_5(OH)_4$					
HTM	T, °C	Element content, at.%			Co/Ge
		Co	Ge	O	
H_2O	100	26.26±0.76	18.31±0.18	55.43±0.79	1.43±0.06
	150	23.73±0.87	18.38±0.12	57.89±0.76	1.29±0.06
	200	26.29±0.70	18.14±0.21	55.57±0.59	1.45±0.06
NaOH	100	23.51±6.36	15.90±1.46	60.59±7.18	1.48±0.54
	150	24.41±0.90	16.68±0.10	58.91±0.84	1.46±0.06
	200	34.39±8.38	14.65±1.11	50.96±7.34	2.35±0.75
Na_2SO_3	100	22.75±0.69	15.09±0.08	62.16±0.75	1.51±0.05
	150	26.32±0.99	17.95±0.18	55.73±0.95	1.47±0.07
	200	27.05±0.94	17.37±0.39	55.58±1.12	1.56±0.09
$Fe_3Si_2O_5(OH)_4$					
HTM	T, °C	Element content, at.%			Fe/Ge
		Fe	Ge	O	
H_2O	100	22.22±0.47	14.82±0.09	62.97±0.41	1.50±0.04
	150	22.41±0.44	15.47±0.14	62.12±0.35	1.45±0.04
	200	45.65±5.66	11.99±1.43	42.36±4.25	3.81±0.93
NaOH	100	26.10±1.28	16.55±0.72	57.35±1.02	1.58±0.15
	150	27.45±1.37	16.33±0.34	56.22±1.22	1.68±0.12
	200	50.16±4.24	10.26±1.27	39.57±3.18	4.89±1.02
Na_2SO_3	100	22.86±0.73	15.41±0.09	61.73±0.77	1.48±0.06
	150	20.22±0.77	15.28±0.16	64.50±0.84	1.32±0.06
	200	27.45±0.81	17.06±0.07	55.49±0.76	1.61±0.05

3.1.3. Fe-phyllogermanate. Unlike the previous phyllogermanates, the main obstacle for Fe-phyllogermanate synthesis is an intensive oxidation of Fe^{2+} to Fe^{3+} during precipitation and hydrothermal treatment. Except paper [42], Fe^{2+}-phyllosilicates with chrysotile or lizardite structure were not obtained, but Fe-phyllosilicate $Fe_{3-2}Si_2O_5(OH)_4$ was obtained with the greenalite structure. The iron in this compound had oxidation states of 2+ and 3+ [43, 44]. Previously obtained $Me_3Ge_2O_5(OH)_4$ phyllogermanates contained divalent metal ions in the octahedral position, so an important task was to stabilize iron in the 2+ oxidation state.

In analogy with other phyllogermanates, Fe-phyllogermanates tended to form phase described by three-layer unit cell in water (Fig. A9, Appendix) because of oriented attachment. Addition of NaOH increased crystallinity (Fig. A8, Appendix) and inhibited the growth along *113* direction. Increase in temperature resulted in the formation of Fe_2O_3 impurity phase. Moreover, Fe-phyllogermanate dehydroxylated with formation of Fe_2GeO_4 and Fe_2O_3 in H_2O and NaOH at 200 °C (using of mother liquor as HTM allowed to obtain single-phase Fe_2GeO_4, see Fig. A11, Appendix). The formation of Fe_2O_3 and Fe_2GeO_4 led to a sharp increase in the Fe/Ge ratio (Table 1) due to the presence in the sample of well-crystallized particles of volumetric shape, from which the signal was most intense and overlapped the signal from particles of smaller size. Addition of Na_2SO_3 prevented Fe_2O_3 and inhibited Fe_2GeO_4 formation at 200 °C (Fig. 1 and Fig. A10, Appendix).

The lattice parameters of Fe-phyllogermanate varied unsystematically (Fig. A12, Appendix), but the unit cell volume did not change significantly with temperature or HTM (Fig. 2g). The crystallite size was about 5 nm for H_2O-HTM samples at $T = 100$ °C, while for Na_2SO_3-HTM and NaOH-HTM samples it was 13 and 11 nm, respectively. The crystallite size increased, reaching about 20 nm at $T = 150$ °C for all HTMs (Fig. 2c). Only Na_2SO_3-HTM retained Fe-phyllogermanate at $T = 200$ °C, the crystallite size was almost 40 nm. Fe-phyllogermanate also had a plate-like morphology, the largest particle size was also characteristic of the H_2O-HTM sample and was about 1 μm at $T = 150$ °C. The same sizes were observed for particles obtained at $T = 200$ °C in the Na_2SO_3-HTM sample. The particles had a size of about 0.5 μm and their size did not change with increasing temperature in NaOH-HTM (Fig. A13(a,b), Appendix).

It is worth noting that the morphology of Fe_2GeO_4 differed significantly depending on HTM. They were plate-like particles similar to Fe-phyllogermanate in the H_2O-HTM sample (Fig. A14a, Appendix). The particles joined into flower-like agglomerates with sizes of 5 μm and larger in the NaOH-HTM sample (Fig. A13c, Appendix), that was probably due to more active particle growth in NaOH-HTM. And in the mother liquor, isomeric particles were formed (Fig. A14b, Appendix). The homogeneity of the composition and distribution of the primary particles, the absence of additional oxidation sources could contribute to this effect.

3.1.4. Co-phyllogermanate. Phases described by two-layer unit cell were formed in all HTMs at $T = 100$ °C, phases described by three-layer unit cells began to form in H_2O-HTM (Fig. A15, Appendix) and Na_2SO_3-HTM (Fig. A16, Appendix) in analogy with previous phyllogermanates. Cobalt orthogermanate Co_2GeO_4 was formed in NaOH-HTM (Fig. A17, Appendix) at 100 °C, which was present in this HTM at all subsequent processing temperatures (Fig. 1). Increasing the temperature to 150 °C resulted in more intense formation of phases described by three-layer unit cells, whereas phases described by two-layer unit cells were practically absent. At $T = 200$ °C only phases described by three-layer unit cells were observed. Growth was observed in the preferred directions *00l*, *h00*, and *113* in all samples with three-layer unit cells, similar to Fe-phyllogermanate, but the texturing effect in these directions was stronger. The lattice parameters remained virtually unchanged at $T = 150$ °C and above, while they changed unsystematically at $T = 100$ °C (Fig. A18, Appendix) comparing different HTMs. The unit cell volume decreased in Na_2SO_3-HTM, while a strong volume decrease occurred in H_2O-HTM (Fig. 2h). While NaOH-HTM promoted the formation of Co-phyllogermanate, the particles in the other two HTMs could be weakly crystallized, resulting in a larger unit cell volume.

Crystallite size increased from an average of 5 nm at $T = 100$ °C to 30 – 40 nm at $T = 150$ °C. Subsequent increased in temperature caused the crystallite size of NaOH-HTM and Na_2SO_3-HTM samples to increase to 45 nm, while the crystallite size in the H_2O-HTM sample remained virtually unchanged (Fig. 2d). The particles were hexagonal plates [19] and had sizes much smaller than the phyllogermanates considered above. The sample contained thin plates of 36 ± 8 nm in size at $T = 100$ °C in the H_2O-HTM sample (Fig. A7c, Appendix). The Co/Ge ratio was kept within the error limits in all samples, except for the Co-phyllogermanate obtained in NaOH-HTM at 200 °C due to the presence of Co2GeO4 in significant amounts, as well as in the sample obtained in H_2O-HTM at 150 °C due to probably strong texturing.

Thus, hydrothermal treatment promoted the formation of phyllogermanates and each series contained single-phase samples, which allowed us to establish the optimal phyllogermanates synthesis parameters. Increase in temperature yielded increase in the number of layers in the unit cell. Neutral pH (H_2O-HTM) enhanced particles attachment with formation of bigger plates. Na_2SO_3-HTM minimized undesirable oxidation of Co^{2+} and Fe^{2+} in hydrothermal conditions.

3.2. Products of heat treatment in Ar–H_2 atmosphere

The reduction of phyllogermanates was carried out in an Ar–H_2 atmosphere to obtain intermetallic compounds or metallic germanium in the case of Mg-phyllogermanate. Single phase samples were selected for the reduction (Fig. 4). The TPR curves are shown in Fig. 5. The reduction took place in one or two stages, depending on the sample. It is worth noting that the shape of the TPR profiles also depended on the H_2O released during the process [45].

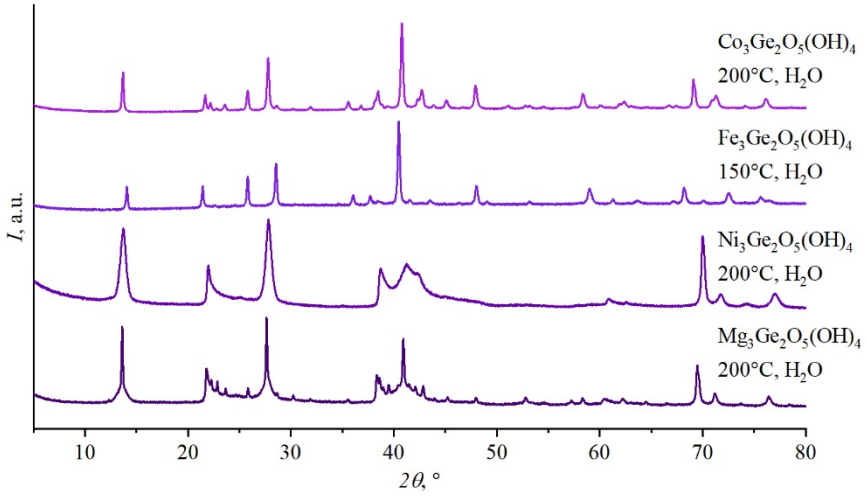

FIG. 4. PXRD patterns of single-phase samples of phyllogermanates obtained in H_2O hydrothermal medium at 150 – 200 °C

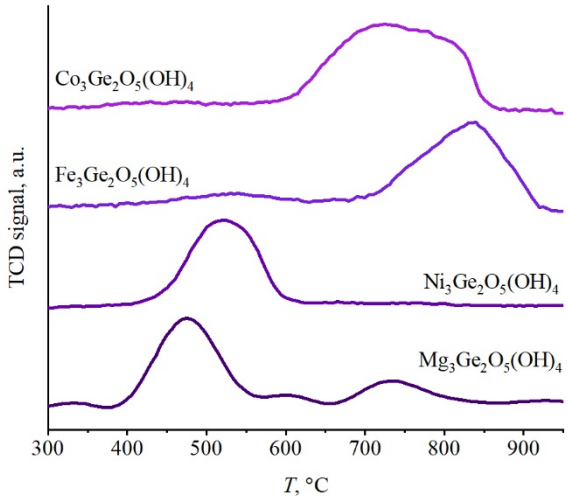

FIG. 5. TPR curves of single-phase samples of phyllogermanates obtained in H_2O hydrothermal medium at 150 – 200 °C

The reduction began at about 400 °C with $T_{\max} = 480$ °C for Mg-phyllogermanate. The second reduction stage started at 665 °C with $T_{\max} = 730$ °C. This was in agreement with literature data on the reduction of GeO_2: hydroxylated GeO_2 had higher reduction temperatures compared to other germanium oxides [46]. Structurally bound water could also affect the reduction process of germanium in the case of Mg-phyllogermanate. Presence of three phases was observed in the sample after the reduction: metallic germanium, orthorhombic Mg_2GeO_4 and cubic Mg_2GeO_4 (Fig. 6). It is possible that the reduction of germanium from phyllogermanate occurred in parallel with the formation of cubic Mg_2GeO_4 and continued until the stoichiometric ratio Mg/Ge = 2 was reached. The increase in temperature contributed to its stabilization and prevented further reduction of germanium from the system. Traditionally, Mg_2GeO_4 is obtained by the solid phase synthesis method [47], therefore the temperatures of its preparation from the corresponding phyllogermanate could be significantly lower. The presence of cubic Mg_2GeO_4 could be associated with an incomplete transition from the cubic to the orthorhombic phase. The second stage of Mg phyllogermanate reduction was weakly intense and could be associated with the phase transition from cubic to orthorhombic Mg_2GeO_4 [48].

The reduction occurred in a single step for Ni-phyllogermanate (Fig. 5), and it was accompanied by the formation of $Ni_{19}Ge_{12}$ intermetallic compound (Fig. 6). It existed in a rather narrow region of the phase diagram. The Ni/Ge ratio in the initial phyllogermanate was 1.5, which was close to the Ni/Ge ratio in the resulting intermetallic compound, and the reduction temperature corresponded exactly to the formation temperature of $Ni_{19}Ge_{12}$ in the phase diagram [49]. The reduction start temperature of Ni-phyllogermanate was 435 °C with a maximum at 520 °C. It was higher than that of Mg-phyllogermanate due to the presence of nickel in the system and the simultaneous reduction of germanium and nickel.

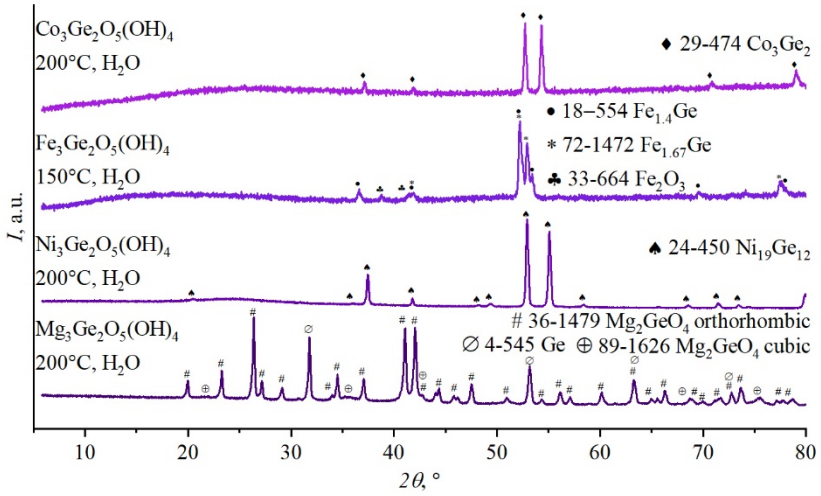

FIG. 6. PXRD patterns of phyllogermanate reduction products in Ar–H_2 (5 % vol. H_2)

The reduction start temperature of Fe-phyllogermanate was 705 °C with $T_{\max} = 845$ °C. This sample had the highest reduction temperature. Structurally bound water greatly slowed down the process of iron reduction [45]. The initial ratio Fe/Ge = 1.5 corresponded to the region of two solid solutions [50], possibly due to this, the formation of two alloys with approximate ratios of $Fe_{1.4}Ge$ and $Fe_{1.67}Ge$ was observed by PXRD (Fig. 6). In addition, a small amount of Fe_2O_3 was present in the sample. This oxide could have formed in air after the reduction process due to the oxidation of metallic iron, which was a reduction product.

The reduction from Co-phyllogermanate occurred in one step (or several steps, indistinguishable due to peaks overlap) with the formation of the intermetallic compound Co_3Ge_2 (Fig. 6), which was a high-temperature phase [51]. The reduction start temperature was 600 °C with a $T_{\max} = 750$ °C, which was higher than the reduction start temperature of a similar phyllosilicate [8]. Apparently, the reduction start temperature increased due to the simultaneous reduction of the transition element and Ge, which led to the destruction of the structure and the formation of the intermetallic compound.

The formation of intermetallic compounds was observed in all samples containing transition elements. Mg-phyllogermanate contained germanium and magnesium orthogermanate. It was possible to obtain intermetallic compounds with a given germanium/transition element ratio by varying the initial *Me*/Ge ratio.

4. Conclusion

Here, we have demonstrated unified approach to Mg-, Ni-, Fe- and Co-phyllogermanates synthesis by soft chemistry methods. Additional precautions to prevent oxidation were required to obtain Co- and Fe-phyllogermanates, so the synthesis was performed in an inert Ar atmosphere using oxygen-free water.

Phyllogermanates tended to form unit cells, the number of layers in which depended on the temperature conditions of the hydrothermal treatment. Ni-phyllogermanate required the highest temperatures to initiate the formation of phases described by three-layer unit cell, while Fe-phyllogermanate required the lowest. The samples were particles with three-layer cells already at 100 °C. Orthogermanates were also formed in Fe- and Co-phyllogermanates under elevated temperature conditions, besides temperature of their formation was much lower than that in the solid phase synthesis method. Therefore, hydrothermal synthesis could be successfully used to obtain not only phyllogermanates, but also orthogermanates.

Temperature-programmed reduction made it possible to estimate the reduction start temperature of germanium in Mg-phyllogermanate and germanium intermetallic compounds in other samples. This method of obtaining intermetallic compounds is quite simple, and the possibility of varying the composition of the initial phyllogermanates to obtain a series of intermetallic compounds with a given ratio makes them promising objects for further research.

Appendix

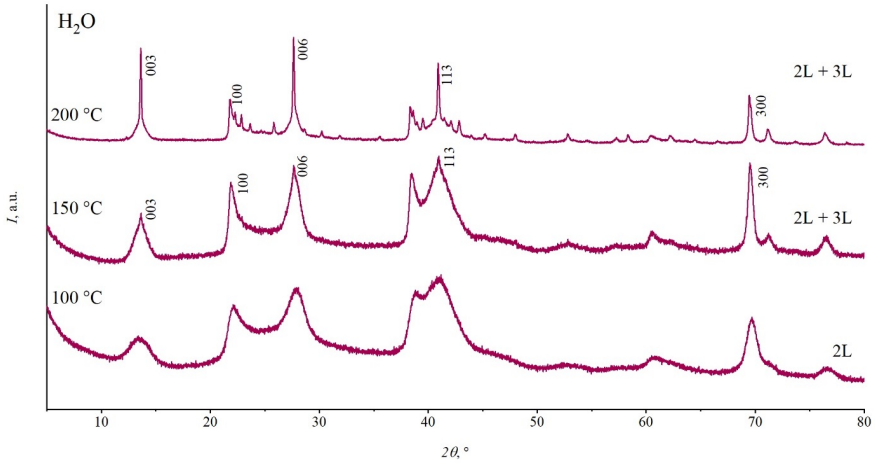

FIG. A1. PXRD patterns of $Mg_3Ge_2O_5(OH)_4$ in H_2O hydrothermal medium at three different temperatures

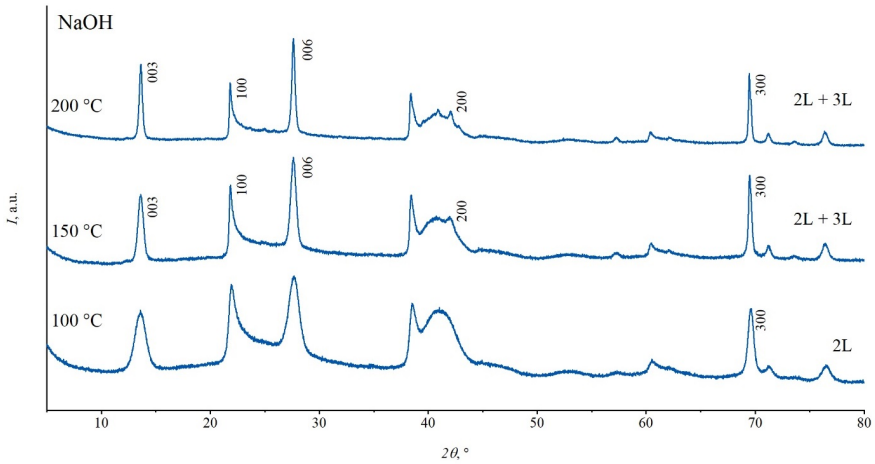

FIG. A2. PXRD patterns of $Mg_3Ge_2O_5(OH)_4$ in NaOH hydrothermal medium at three different temperatures

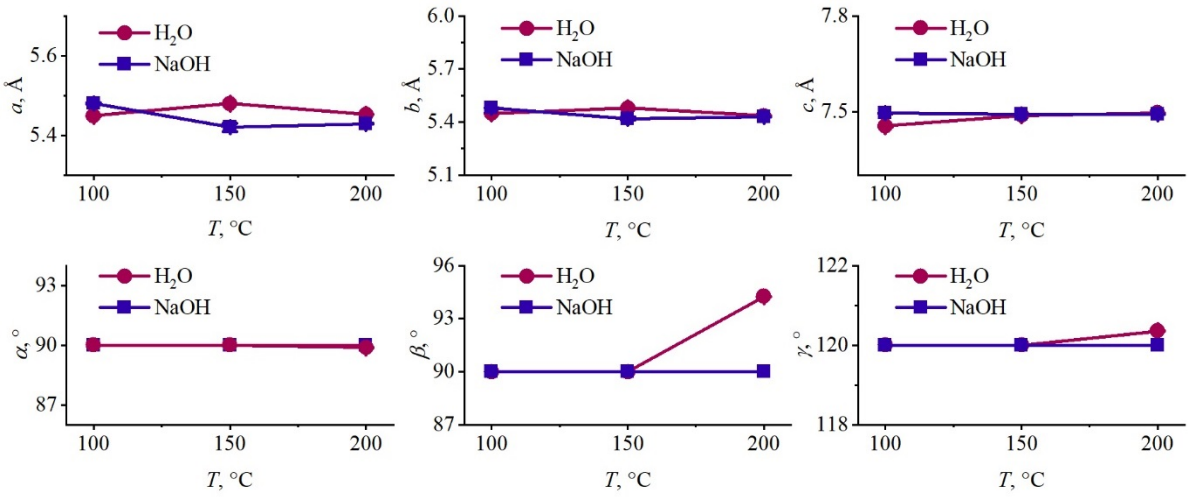

FIG. A3. Lattice parameters of $Mg_3Ge_2O_5(OH)_4$ in H_2O and NaOH hydrothermal media at three different temperatures

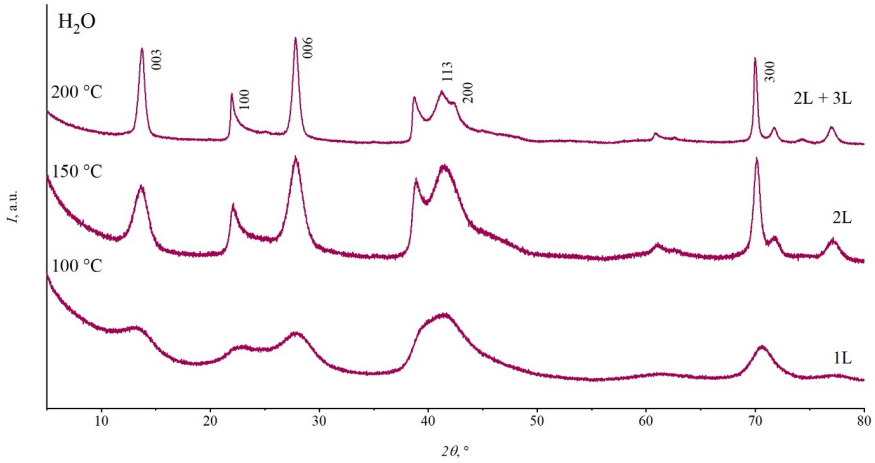

FIG. A4. PXRD patterns of $Ni_3Ge_2O_5(OH)_4$ in H_2O hydrothermal medium at three different temperatures

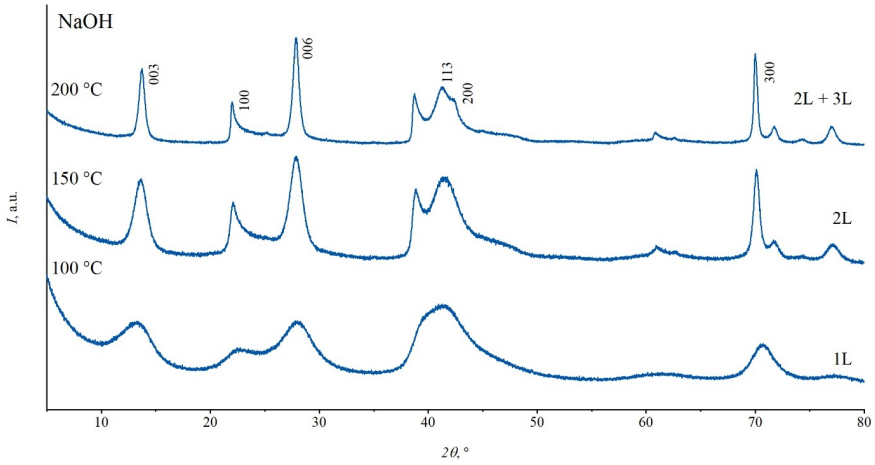

FIG. A5. PXRD patterns of $Ni_3Ge_2O_5(OH)_4$ in NaOH hydrothermal medium at three different temperatures

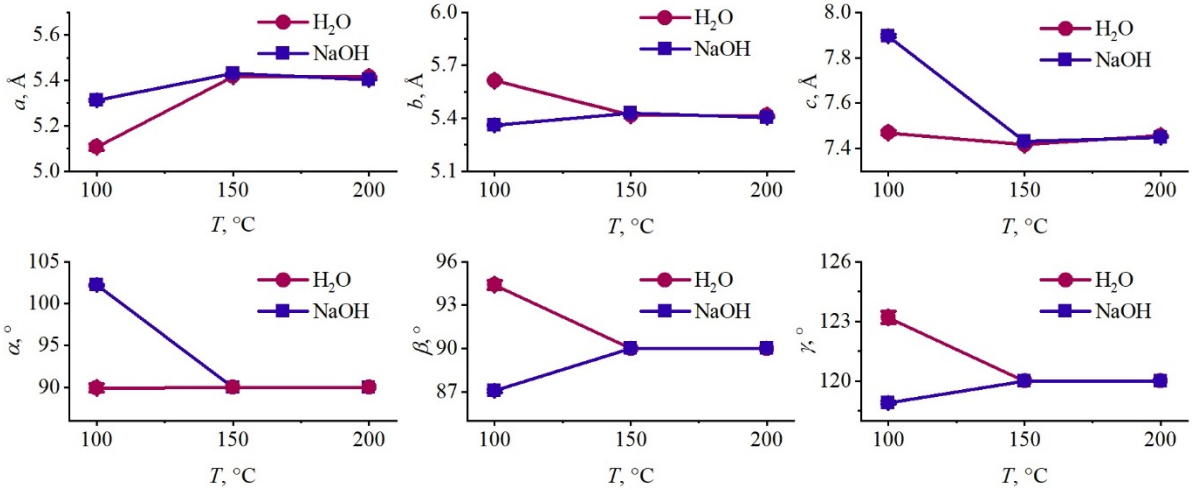

FIG. A6. Lattice parameters of $Ni_3Ge_2O_5(OH)_4$ in H_2O and NaOH hydrothermal media at three different temperatures

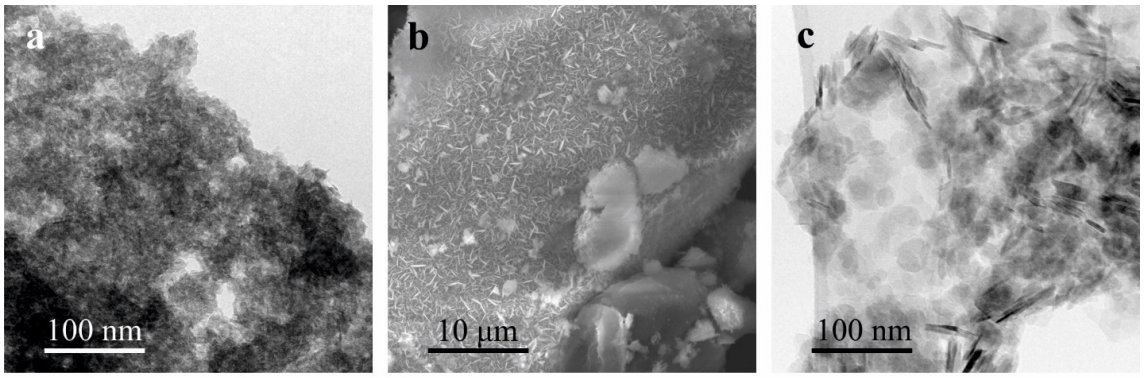

FIG. A7. a) TEM micrograph of $Ni_3Ge_2O_5(OH)_4$ at 100 °C in NaOH hydrothermal medium; b) SEM micrograph of $Ni_3Ge_2O_5(OH)_4$ at 200 °C in H_2O hydrothermal medium; and c) TEM micrographs of $Co_3Ge_2O_5(OH)_4$ at 100 °C in H_2O hydrothermal medium

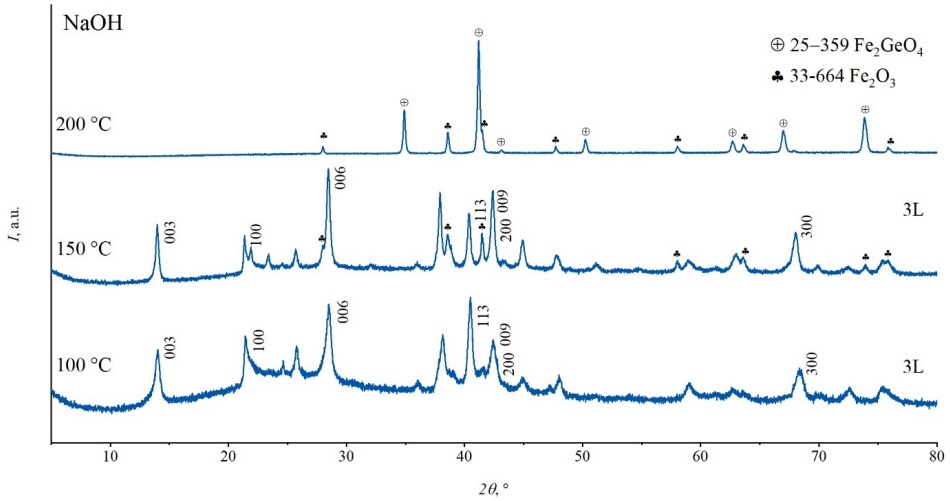

FIG. A8. PXRD patterns of $Fe_3Ge_2O_5(OH)_4$ in NaOH hydrothermal medium at three different temperatures

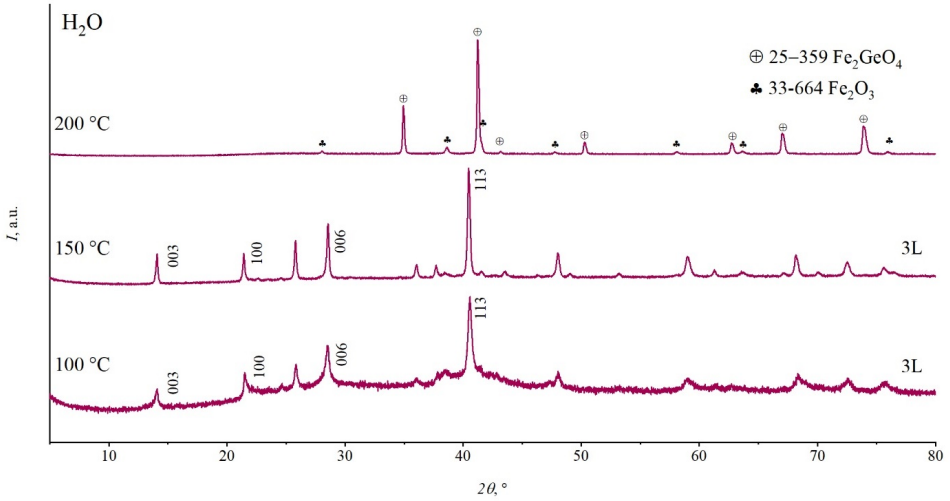

FIG. A9. PXRD patterns of $Fe_3Ge_2O_5(OH)_4$ in H_2O hydrothermal medium at three different temperatures

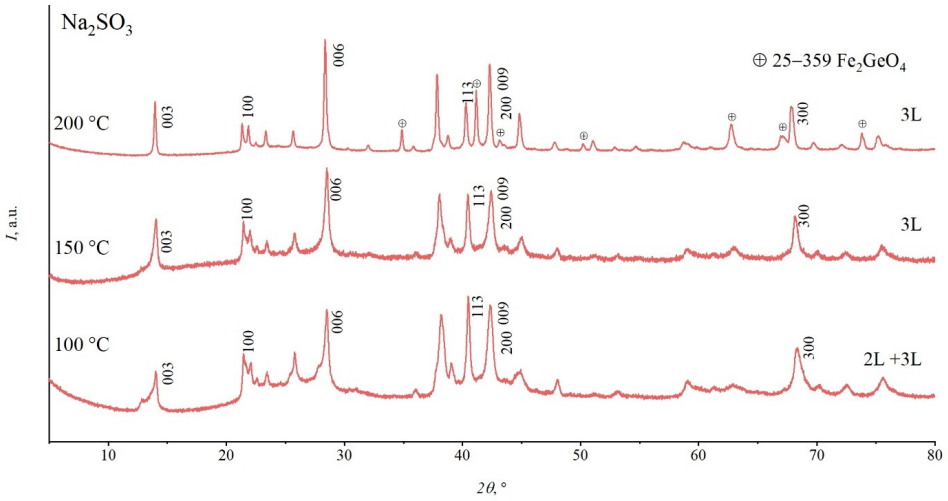

FIG. A10. PXRD patterns of $Fe_3Ge_2O_5(OH)_4$ in Na_2SO_3 hydrothermal medium at three different temperatures

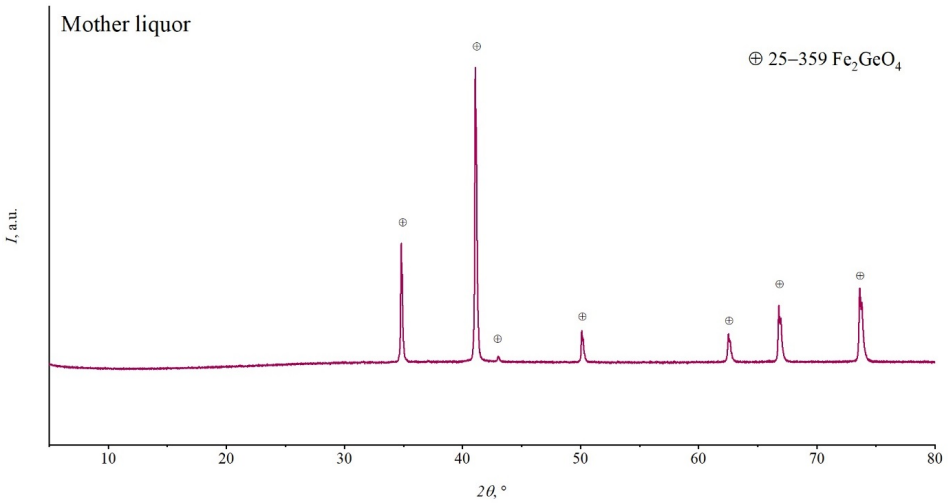

FIG. A11. PXRD pattern of $Fe_3Ge_2O_5(OH)_4$ treated in mother liquor at 200 °C

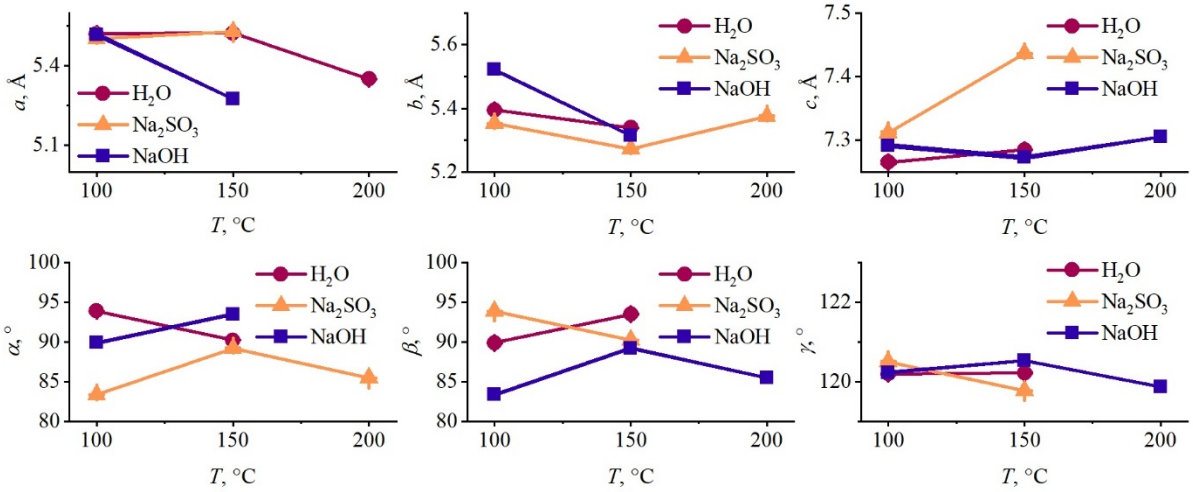

FIG. A12. Lattice parameters of $Fe_3Ge_2O_5(OH)_4$ in H_2O, NaOH and Na_2SO_3 hydrothermal media at three different temperatures

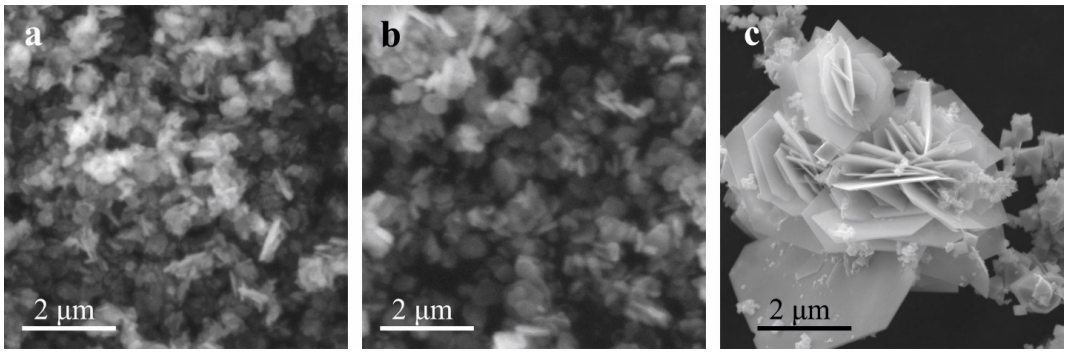

FIG. A13. SEM micrographs of $Fe_3Ge_2O_5(OH)_4$ in NaOH hydrothermal medium: a) at 100 °C; b) at 150 °C; c) at 200 °C

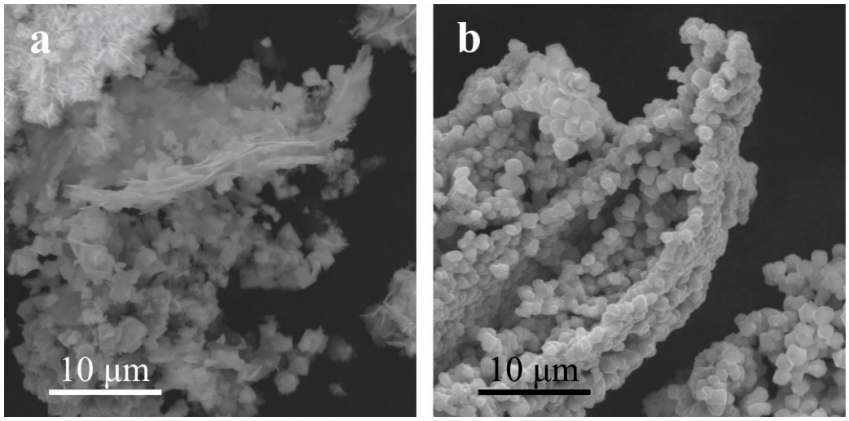

FIG. A14. SEM micrographs of $Fe_3Ge_2O_5(OH)_4$ at 200 °C a) in H_2O hydrothermal medium; b) in mother liquor

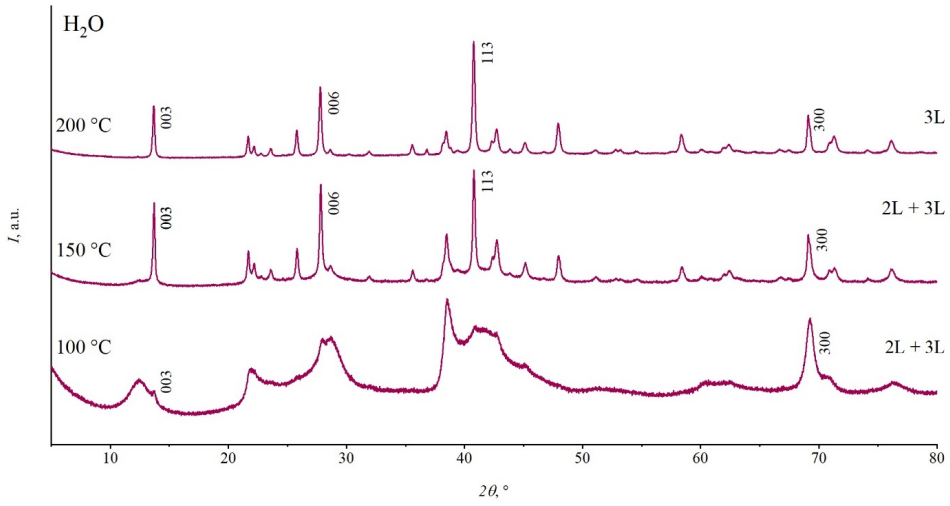

FIG. A15. PXRD patterns of $Co_3Ge_2O_5(OH)_4$ in H_2O hydrothermal medium at three different temperatures

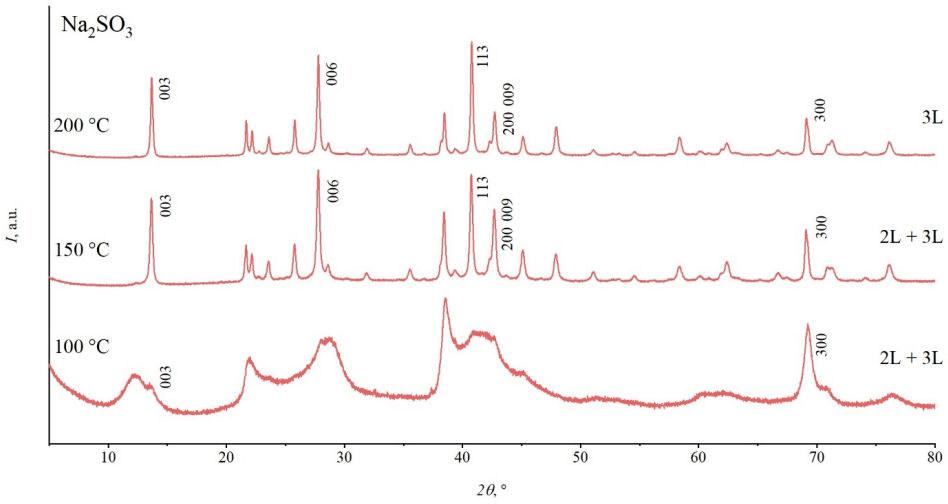

FIG. A16. PXRD patterns of $Co_3Ge_2O_5(OH)_4$ in Na_2SO_3 hydrothermal medium at three different temperatures

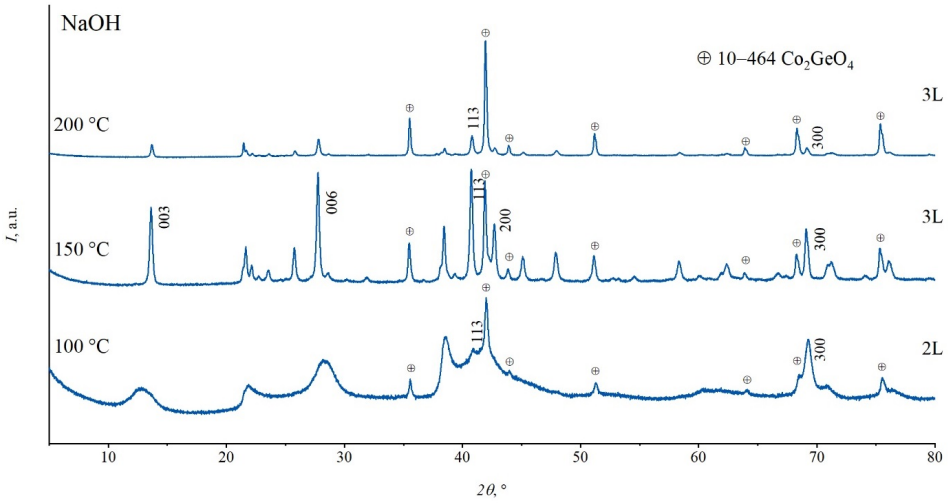

FIG. A17. PXRD patterns of $Co_3Ge_2O_5(OH)_4$ in NaOH hydrothermal medium at three different temperatures

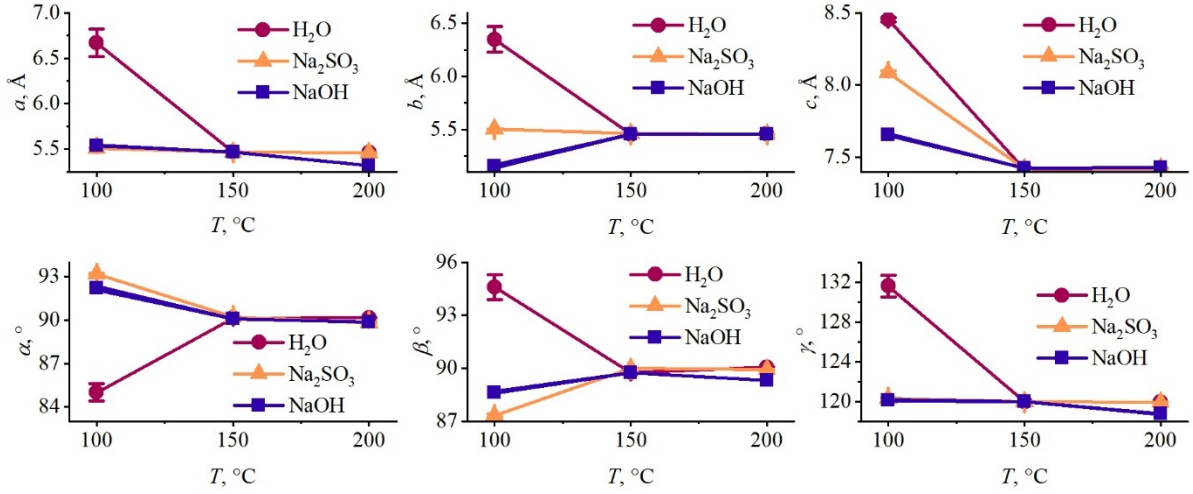

FIG. A18. Lattice parameters of $Co_3Ge_2O_5(OH)_4$ in H_2O, NaOH and Na_2SO_3 hydrothermal media at three different temperatures

References

[1] Roveri N., Falini G., Foresti E., Fracasso G., Lesci I.G., Sabatino P. Geoinspired synthetic chrysotile nanotubes. *J. of materials research*, 2006, **21** (11), P. 2711–2725.

[2] Korytkova E.N., Maslov A.V., Pivovarova L.N., Drozdova I.A., Gusarov V.V. Formation of $Mg_3Si_2O_5(OH)_4$ nanotubes under hydrothermal conditions. *Glass Physics and Chemistry*, 2004, **30**, P. 51–55.

[3] Mellini M. The crystal structure of lizardite 1 T: hydrogen bonds and polytypism. *American Mineralogist*, 1982, **67** (5–6), P. 587–598.

[4] Alvarez-Ramírez F., Toledo-Antonio J.A., Angeles-Chavez C., Guerrero-Abreo J.H., López-Salinas E. Complete structural characterization of Ni3$Si_2O_5(OH)_4$ nanotubes: theoretical and experimental comparison. *The J. of Physical Chemistry C*, 2011, **115** (23), P. 11442–11446.

[5] Krasilin A.A., Semenova A.S., Kellerman D.G., Nevedomsky V.N., Gusarov V.V. Magnetic properties of synthetic $Ni_3Si_2O_5(OH)_4$ nanotubes. *Europhysics Letters*, 2016, **113** (4), 47006.

[6] Korytkova E.N., Maslov A.V., Pivovarova L.N., Polegotchenkova Y.V., Povinich V.F., Gusarov V.V. Synthesis of nanotubular $Mg_3Si_2O_5(OH)_4$–$Ni_3Si_2O_5(OH)_4$ silicates at elevated temperatures and pressures. *Inorganic materials*, 2005, **41**, P. 743–749.

[7] Korytkova E.N., Pivovarova L.N. Hydrothermal synthesis of nanotubes based on (Mg, Fe, Co, Ni)$_3Si_2O_5(OH)_4$ hydrosilicates. *Glass Physics and Chemistry*, 2010, **36**, P. 53–60.

[8] Khrapova E.K., Ivanova A.A., Kirilenko D.A., Levin A.A., Bert N.A., Ugolkov V.L., Krasilin A.A. Phase transformations of $(Co_xMg_{1-x})_3Si_2O_5(OH)_4$ phyllosilicate nanoscrolls upon heating in Ar, O_2 and H_2 containing atmospheres. *Applied Clay Science*, 2024, **250**, 107282.

[9] Khrapova E.K., Kozlov D.A., Krasilin A.A. Hydrothermal Synthesis of Hydrosilicate Nanoscrolls $(Mg_{1-x}Co_x)_3Si_2O_5(OH)_4$ in a Na_2SO_3 Solution. *Russian J. of Inorganic Chemistry*, 2022, **67** (6), P. 839–849.

[10] Korytkova E.N., Pivovarova L.N., Gusarov V.V. Influence of iron on the kinetics of formation of chrysotile nanotubes of composition (Mg, Fe)$_3Si_2O_5(OH)_4$ under hydrothermal conditions. *Geochemistry International*, 2007, **45**, P. 825–831.

[11] Krasilin A.A., Panchuk V.V., Semenov V.G., Gusarov V.V. Formation of variable-composition iron (III) hydrosilicates with the chrysotile structure. *Russian J. of General Chemistry*, 2016, **86**, P. 2581–2588.

[12] Foresti E., Hochella Jr M.F., Kornishi H., Lesci I.G., Madden A.S., Roveri N., Xu H. Morphological and Chemical/Physical Characterization of Fe-Doped Synthetic Chrysotile Nanotubes. *Advanced Functional Materials*, 2005, **15** (6), P. 1009–1016.

[13] Bloise A., Barrese E., Apollaro C. Hydrothermal alteration of Ti-doped forsterite to chrysotile and characterization of the resulting chrysotile fibers. *Neues Jahrbuch für Mineralogie*, 2009, **185** (3), P. 297–304.

[14] Roy D.M., Roy R. An experimental study of the formation and properties of synthetic serpentines and related layer silicate minerals. *American Mineralogist: J. of Earth and Planetary Materials*, 1954, **39** (11–12), P. 957–975.

[15] Krasilin A.A., Khrapova E. K. Effect of hydrothermal treatment conditions on formation of nickel hydrogermanate with platy morphology. *Russian J. of Applied Chemistry*, 2017, **90**, P. 22–27.

[16] White R.D., Bavykin D.V., Walsh F.C. Spontaneous scrolling of kaolinite nanosheets into halloysite nanotubes in an aqueous suspension in the presence of GeO_2. *The J. of Physical Chemistry C*, 2012, **116** (15), P. 8824–8833.

[17] Paineau E. Imogolite nanotubes: a flexible nanoplatform with multipurpose applications. *Applied Sciences*, 2018, **8** (10), 1921.

[18] Hall S.H., Guggenheim S., Moore P., Bailey S.W. The structure of Unst-type 6-layer serpentines. *The Canadian Mineralogist*, 1976, **14** (3), P. 314–321.

[19] Belskaya N.A., Khrapova E.K., Ivanova A.A., Eremin E.V., Pavlov S.I., Krasilin A.A. Structure refinement and magnetic properties of synthetic $Co_3Ge_2O_5(OH)_4$ phyllogermanate. *J. of Magnetism and Magnetic Materials*, 2023, **587**, 171262.

[20] Abdelkrim Y., Wu J., Jiao F.Z., Wang Z.H., Hou S.X., Zhang T.T., Qu J. Cobalt germanium hydroxides with asymmetric electron distribution and surface hydroxyl groups for superb catalytic degradation performances. *J. of Colloid and Interface Science*, 2025, **677**, P. 282–293.

[21] Xu Z., Li W., Wang X., Wang B., Shi Z., Dong C., Zou Z. Novel cobalt germanium hydroxide for electrochemical water oxidation. *ACS applied materials & interfaces*, 2018, **10** (36), P. 30357–30366.

[22] Zhang N., Yang B., He Y., He Y., Liu X., Liu M., Roy V.A. Serpentine $Ni_3Ge_2O_5(OH)_4$ nanosheets with tailored layers and size for efficient oxygen evolution reactions. *Small*, 2018, **14** (48), 1803015.

[23] Yang B., Zhang N., Chen G., Liu K., Yang J., Pan A., Qiu T. Serpentine $Co_xNi_{3-x}Ge_2O_5(OH)_4$ nanosheets with tuned electronic energy bands for highly efficient oxygen evolution reaction in alkaline and neutral electrolytes. *Applied Catalysis B: Environmental*, 2020, **260**, 118184.

[24] Wen N., Chen S., Feng J., Zhang K., Zhou Z., Li X., Zhao Y. In situ hydrothermal synthesis of double-carbon enhanced novel cobalt germanium hydroxide composites as promising anode material for sodium ion batteries. *Dalton transactions*, 2021, **50** (12), P. 4288–4299.

[25] Li H.S., Qu J., Hao S.M., Wang Z.Z., Zhang Y.J., Yu Z.Z. Enhanced lithium storage performances of novel layered nickel germanate anodes inspired by the spatial arrangement of lotus leaves. *Nanoscale*, 2018, **10** (23), P. 10963–10970.

[26] Liu F., Ye S., Guo H., Zhai M., Qian J. Assembled β-Co$(OH)_2$ Nanoparticles on Reduced Graphene Oxide for Enhanced Magnetism. *J. of Superconductivity and Novel Magnetism*, 2014, **27**, P. 787–791.

[27] Gaudet S., Detavernier C., Kellock A.J., Desjardins P., Lavoie C. Thin film reaction of transition metals with germanium. *J. of Vacuum Science & Technology A*, 2006, **24** (3), P. 474–485.

[28] Sadoh T., Kamizuru H., Kenjo A., Miyao M. Low-temperature formation ($< 500\ ^\circ$ C) of poly-Ge thin-film transistor with NiGe Schottky source/drain. *Applied physics letters*, 2006, **89** (19).

[29] Kauzlarich S.M., Ju Z., Tseng E., Lundervold J. Recent developments in germanium containing clusters in intermetallics and nanocrystals. *Chemical Society Reviews*, 2021, **50** (23), P. 13236–13252.

[30] Menezes P.W., Yao S., Beltrán?Suito R., Hausmann J.N., Menezes P.V., Driess M. Facile access to an active γ-NiOOH electrocatalyst for durable water oxidation derived from an intermetallic nickel germanide precursor. *Angewandte Chemie*, 2021, **133** (9), P. 4690–4697.

[31] Walter C., Menezes P. W., Driess M. Perspective on intermetallics towards efficient electrocatalytic water-splitting. *Chemical Science*, 2021, **12** (25), P. 8603–8631.

[32] Toraya H. Quantitative phase analysis using observed integrated intensities and chemical composition data of individual crystalline phases: quantification of materials with indefinite chemical compositions. *J. of Applied Crystallography*, 2017, **50** (3), P. 820–829.

[33] Toraya H. Whole-powder-pattern fitting without reference to a structural model: application to X-ray powder diffraction data. *J. of Applied Crystallography*, 1986, **19** (6), P. 440–447.

[34] Schneider C.A., Rasband W.S., Eliceiri K.W. NIH Image to ImageJ: 25 years of image analysis. *Nature methods*, 2012, **9** (7), P. 671–675.

[35] Ivanov V.K., Fedorov P.P., Baranchikov A.Y., Osiko V.V.E. Oriented attachment of particles: 100 years of investigations of non-classical crystal growth. *Russian Chemical Reviews*, 2014, **83** (12), 1204.

[36] Pokrovski G.S., Schott J. Thermodynamic properties of aqueous Ge (IV) hydroxide complexes from 25 to 350 C: implications for the behavior of germanium and the Ge/Si ratio in hydrothermal fluids. *Geochimica et Cosmochimica Acta*, 1998, **62** (9), P. 1631–1642.
[37] Lin J.X., Wang L. Adsorption of dyes using magnesium hydroxide-modified diatomite. *Desalination and Water Treatment*, 2009, **8** (1–3), P. 263–271.
[38] Hernández N., Moreno R., Sánchez-Herencia A.J., Fierro J.L. Surface behavior of nickel powders in aqueous suspensions. *The J. of Physical Chemistry B*, 2005, **109** (10), P. 4470–4474.
[39] Lorenzen A.L., Rossi T.S., Riegel-Vidotti I.C., Vidotti M. Influence of cationic and anionic micelles in the (sono) chemical synthesis of stable $Ni(OH)_2$ nanoparticles: "In situ" zeta-potential measurements and electrochemical properties. *Applied Surface Science*, 2018, **455**, P. 357–366.
[40] White R.D., Bavykin D.V., Walsh F.C. Morphological control of synthetic $Ni_3Si_2O_5(OH)_4$ nanotubes in an alkaline hydrothermal environment. *J. of Materials Chemistry A*, 2013, **1** (3), P. 548–556.
[41] Krasilin A.A., Nevedomsky V.N., Gusarov V.V. Comparative energy modeling of multiwalled $Mg_3Si_2O_5(OH)_4$ and $Ni_3Si_2O_5(OH)_4$ nanoscroll growth. *The J. of Physical Chemistry C*, **121** (22), P. 12495–12502.
[42] Bloise A., Belluso E., Barrese E., Miriello D., Apollaro C. Synthesis of Fe-doped chrysotile and characterization of the resulting chrysotile fibers. *Crystal Research and Technology: J. of Experimental and Industrial Crystallography*. **44** (6), P. 590–596.
[43] Dzene L., Brendle J., Limousy L., Dutournie P., Martin C., Michau N. Synthesis of iron-rich tri-octahedral clay minerals: A review. *Applied Clay Science*, 2018, **166**, P. 276–287.
[44] Pignatelli I., Mosser-Ruck R., Mugnaioli E., Sterpenich J., Gemmi M. The effect of the starting mineralogical mixture on the nature of Fe-serpentines obtained during hydrothermal synthesis at 90 C. *Clays and Clay Minerals*, 2020, **68** (4), P. 394–412.
[45] Zieliñski J., Zglinicka I., Znak L., Kaszkur Z. Reduction of Fe_2O_3 with hydrogen. *Applied Catalysis A: General*, 2010, **381** (1–2), P. 191–196.
[46] Bielz T., Soisuwan S., Girgsdies F., Klo?tzer B., Penner S. Reduction of different GeO_2 polymorphs. *The J. of Physical Chemistry C*, 2012, **116** (18), P. 9961–9968.
[47] Chen C.X., Wu S.P., Fan Y.X. Synthesis and microwave dielectric properties of B_2O_3-doped Mg_2GeO_4 ceramics. *J. of alloys and compounds*, 2013, **578**, P. 153–156.
[48] Yamaguchi O., Matumoto H., Morikawa S., Shimizu K. Preparation and Thermal Behavior of Magnesium?Germanium Hydroxide. *J. of the American Ceramic Society*, 1983, **66** (9), P. c169–c170.
[49] Liu Y.Q., Ma D.J., Du Y. Thermodynamic modeling of the germanium–nickel system. *J. of Alloys and Compounds*, 2010, **491** (1–2), P. 63–71.
[50] Okamoto H. Fe–Ge (iron-germanium). *J. of Phase Equilibria and Diffusion*, 2008, **29** (3), 292.
[51] Audebrand N., Ellner M., Mittemeijer E J. High-temperature ordering of structural vacancies in the cobalt-rich portion of the binary system Co–Ge. *J. of alloys and compounds*, 2005, **388** (2), P. 230–234.

Submitted 15 November 2024; accepted 25 November 2024

Information about the authors:

Ekaterina K. Khrapova – Ioffe Institute, 194021 St. Petersburg, Russia; ORCID 0000-0003-2674-9653; e.k.khrapova@mail.ioffe.ru

Anastasia A. Ivanova – Ioffe Institute, 194021 St. Petersburg, Russia; ORCID 0000-0002-8134-1506; a.a.ivanova@mail.ioffe.ru

Demid A. Kirilenko – Ioffe Institute, 194021 St. Petersburg, Russia; ORCID 0000-0002-1571-209X; demid.kirilenko@mail.ioffe.ru

Andrei A. Krasilin – Ioffe Institute, 194021 St. Petersburg, Russia; ORCID 0000-0002-3938-3024; ikrasilin@mail.ioffe.ru

Conflict of interest: the authors declare no conflict of interest.